APL Photonics

Integrated vortex beam emitter in the THz frequency range: design and simulation

Hailong Pi[1], Tasmiat Rahman[1], Stuart A. Boden[1], Tianjun Ma[2], Jize Yan[1] and Xu Fang[1]*

[1]School of Electronics and Computer Science, University of Southampton, SO17 1BJ, UK

[2]Aerospace Information Research Institute, Chinese Academy of Sciences, Beijing 100094, China

*x.fang@soton.ac.uk

Abstract:

Compact vortex beam emitters have emerged as new light sources for novel applications in areas including spectroscopy, particle manipulation and communications. Reported devices depend on linear optical phenomena and emit light in the near-infrared regime. Here, we propose and numerically evaluate a nonlinear vortex beam emitter that functions in the THz regime. The design utilises a $LiNbO_3$ microring, a Si microdisk, and a Au second-order top grating to convert waveguide-coupled infrared light into a freely propagating THz beam via difference-frequency generation. The output beam carries a topological charge that is tuneable with input wavelengths. Three devices are evaluated in a test frequency range from 9 THz to 13.5 THz, and the topological charge can change from -2 to 4. A frequency shift accompanies the change in the topological charge, and its magnitude depends on the planar dimensions of the emitter.

I. Introduction

Light beams carrying orbital angular momentum (OAM), which are also termed as vortex or Laguerre-Gaussian light beams, have a helical phase front.[1] The twist of the helical is quantified by the topological charge, with its sign and amplitude describing the direction and the strength of the twist, respectively. A unique property of the vortex light beams is that the topological charge can take a wide, theoretically unbounded, range of integer and fractional numbers.[2] It allows for a wide variety of intriguing phase and intensity distributions that are unavailable to conventional Hermite-Gaussian light beams. This property also underpins a range of emerging applications including detection of magnetic excitation and enantiomers,[3,4] phase-contrast microscopy,[5] holographic optical manipulation,[6] and high-capacity optical data communications.[7,8]

The creation of vortex beams is the crucial first step of OAM research and has been widely studied. Most methods rely on using judiciously designed optical elements to impart, in either a linear or a nonlinear process, topological charges to a conventional, freely propagating Hermite-Gaussian beam. These elements include cylindrical lenses, spiral phase plates, computer-generated holograms, liquid crystal q-plates,[9] segmented half-wave plates,[10] plasmonic nanostructures[11] and metasurfaces.[12-15] This approach of conversion from a Hermite-Gaussian to a Laguerre-Gaussian mode imposes inherent limitations on several key operating parameters such as speed, efficiency and footprint. For many applications, recent advances of integrated OAM light emitters represent a better solution: the topological charge is created at the stage of light emission, eliminating the need of any subsequent light-conversion element.[16] However, these vortex beam emitters radiate light only in the near-infrared regime, at wavelengths between 0.8 μm and 1.8 μm. The spectral range is restricted by either the transmission window of the integrated photonics platforms or the spectral range of the emitter. In particular, an integrated THz light source that allows for both the generation and tuning of OAM is, to the best of our knowledge, not yet available.

This work proposes and numerically evaluates a vortex beam emitter that functions in the THz (terahertz), an electromagnetic range that is being explored for a range of novel applications.[17] Recent

advances in THz research, e.g. THz wireless communications and THz-driven electron acceleration, have made the development of a compact, surface-emitting THz vortex beam source highly desirable.[18,19] This work introduces a nonlinear, tuneable vortex beam emitter that could be useful in many of these emerging applications. By utilising resonance-enhanced difference-frequency generation, the device retains the compact size of previously reported vortex beam emitters whilst also extending the functional regime into the THz. The integration of photonics and THz research has witnessed the use of nano- and microstructures at every stage of THz generation, propagation, modulation and detection.[20-22] This work demonstrates a new approach of the integration that allows for creating a tuneable topological charge in the generation of THz light.

II. Design of the vortex beam emitter

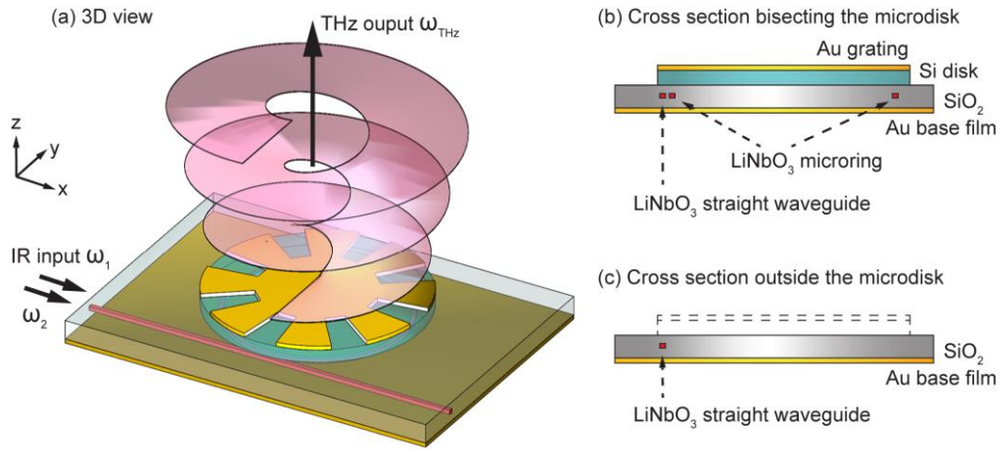

Fig. 1. Schematic of the proposed THz light source. (a) Two infrared (IR) pump waves with angular frequencies ω_1 and ω_2 are coupled into a $LiNbO_3$ microring resonator via a $LiNbO_3$ bus waveguide. Both the microring and the bus waveguide are embedded in a SiO_2 cladding film, which is on top of a planar Au base film. A Si microdisk and a Au circular grating are on top of the microring, and these three components are concentric. The device converts the two waveguide-confined pump waves into a freely propagating THz wave. The THz wave is radiated outwards from the Au grating output-coupler, carrying a tuneable topological charge. (b) Device cross section bisecting the microdisk. (c) Device

cross section outside the microdisk, with the edges of the Si microdisk and the Au grating shown in dashed lines.

Figure 1 illustrates the microstructures of the THz vortex beam emitter. The emitter is a waveguide-coupled, multi-layered microdisk that converts two infrared waveguide modes into free-space THz light through the nonlinear process of difference-frequency generation. $LiNbO_3$ (lithium niobate) is chosen as the waveguide material because of its high nonlinear coefficient[23-26] and increasing importance in integrated photonic circuits.[27,28] The waveguides have two segments, a straight bus waveguide and a microring resonator. They are in the same plane, and have the same rectangular cross section that is 1 μm in width and 800 nm in height. The microring has a bend radius, defined as being from the inner boundary of the waveguide, of 18.68 μm, and a gap with the straight waveguide of 200 nm. The $LiNbO_3$ waveguides are embedded in a SiO_2 cladding layer, a common configuration of lithium niobate on insulator (LNOI) platforms.[27,28] The thickness of the cladding layer is 4.6 μm in total and 2 μm beneath the $LiNbO_3$ waveguides. The bottom of the SiO_2 layer is fully covered by an unstructured Au base film, which has a thickness of 1 μm. A Si microdisk and a Au angular grating, which are concentric to the $LiNbO_3$ microring, are on top of the SiO_2 layer. The Si microdisk has a radius of 22 μm and a thickness of 3 μm. The Au angular grating on top of it has 8 periodic elements, an outer radius of 22 μm, and a thickness of 1 μm. Each of the 8 notches has a depth of 10 μm, an open angle of 200°, and a flat base with a width of 4 μm. These dimensions are further specified in the Supplementary Material (Fig. S1).

The THz emitter is pumped by two infrared light beams with angular frequencies of ω_1 and ω_2. The infrared light is evanescently coupled from the straight waveguide into the ring waveguide, where it forms whispering gallery mode resonances. Due to the resonance enhancement, the microring has a levitated effective nonlinear efficiency[29,30] in the generation of the THz light ω_{THz}, where $\omega_{THz} = \omega_1 - \omega_2$. It is worth noting that, the microring configuration can be used to enhance many different nonlinear processes, among which difference-frequency generation is the only second-order nonlinear process that generates THz light. As shown below, similar to the pump light circulating along the $LiNbO_3$ microring, the THz light can form a whispering gallery mode that traces the circumference of the Si

APL Photonics

microdisk. The THz light is further confined by the Au angular grating at the top and the unstructured Au base film at the bottom, and leaky radiation from this subwavelength-thick cavity forms the output beam. As the unstructured Au base film, a closed end of the leaky cavity, blocks any emission downwards, only the radiation above the emitter is studied.

A key aspect of the design in the generation of topological charge is the Au top grating. Top gratings have been used on a variety of light sources, such as light-emitting diodes (LEDs)[31], vertical-cavity surface-emitting lasers (VCSELs)[32] and quantum cascade lasers (QCLs).[33,34] These gratings can control both the local optical density of states and the flow of light, and are adopted mainly for improving the efficiency and the directionality of light emission. More recently, second-order surface gratings with rotational symmetry have been used to create vortex beams in linear light emitters.[35-40] In contrast to these recent works, which are all in the near-infrared regime, this work adopts a different type of surface grating for use in the THz regime: it is metallic and covers a large area of the top surface of the light emitter. This approach benefits from the low ohmic loss in metals in the THz regime as compared to the near-infrared regime. It can also suppress direct light emission (i.e. emission that bypasses any interactions with a top grating) that can hinder the generation of pure vortex modes.

The performance of the device was numerically evaluated by using a commercial FDTD (finite-difference time-domain) solver (Lumerical FDTD Solutions). For linear properties, the permittivity of the materials, including $LiNbO_3$, SiO_2, Si and Au, was fitted based on experimental values.[41,42] The fitting covered the whole range from the infrared to the THz, and satisfied the Kramers-Kronig relations as required by the FDTD method (see Table S1 in the Supplementary Material for representative values). $LiNbO_3$ was the only nonlinear material in the device, and its nonlinear coefficient[23-26] was set as d_{33} = 170 pm/V. The two input infrared waves had equal power and were launched 40 μm away from the 200 nm gap (i.e. the location where the microring and the straight waveguide were the closest). Both waves were polarised in the same direction (TM polarisation, magnetic field parallel to the substrate) in the *z*-cut $LiNbO_3$ waveguides, in order to access this coefficient. Although this polarisation configuration forbids birefringence phase matching, quasi-phase matching could be used in future

works to boost nonlinear efficiency (e.g. via decorating the microring with nanostructures). To elucidate the mechanism of the creation of topological charge, the results in the main text were obtained by eliminating the nonlinear generation in the straight waveguide. This modification enables establishing a clear link between the near-field distribution and the far-field radiation, and results without this modification are presented in Fig. S2 in the Supplementary Material as a comparison.

III. Input properties of the device

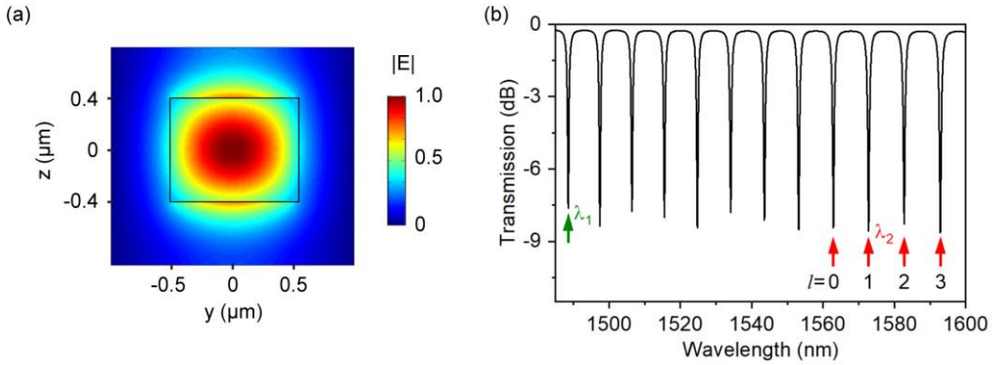

Fig. 2. Properties of the straight waveguide at input wavelengths. (a) Electric field profile of the waveguide mode in the $LiNbO_3$ waveguide (black rectangle) and the SiO_2 layer. The field magnitude is normalised against its maximum value. The map shows the distribution at wavelength λ_1 = 1488.56 nm, and remains almost unchanged over the entire spectral range of panel (b). (b) Transmission spectrum of the waveguide. One of the input wavelengths is fixed (λ_1, green arrow), while the other input wavelength λ_2 is tuned (red arrows), in order to change the topological charge *l* of the radiated THz light.

Figure 2 shows the properties of the device at the pump wavelengths, i.e. in the infrared regime. To maximise the nonlinear conversion efficiency, the cross section of the waveguide is designed to create a TM mode profile with most of the energy confined inside the waveguide (Fig. 2a). Figure 2b shows light transmission through the straight waveguide after passing by the microring resonator. A series of sharp dips are observed in the transmission spectrum, each corresponding to the formation of a whispering gallery resonance mode in the microring. The loaded quality factor of the resonances is ~3.2 $\times 10^3$ at λ_1 = 1488.56 nm as determined using Lorentz fitting,[43] with the material loss attributed as the

main limiting factor. The average transmission is -8.3 dB at λ_1 and λ_2, and the average coupling efficiency is 85% under the assumption of zero scattering loss at the coupling section.[29] The wavelengths of the two input light beams are set at these resonances, in order to benefit from the resonance enhancement of nonlinear effects in the microring.

IV. Generation of topological charges

The input light is confined by the $LiNbO_3$ waveguide and the SiO_2 embedding layer, which dictate the input properties of the device. In contrast, the THz light generated inside the $LiNbO_3$ microring has a much longer wavelength (~25 μm in free space) and penetrates into the Si microdisk. As shown in Fig. 3a, a Si microdisk with proper dimensions supports a whispering gallery mode for the THz light. The conservation of orbital momentum[30,44] in difference-frequency generation requires the confined THz light to obey the condition of

$$m_{THz} = m_1 - m_2 \qquad (1)$$

where m_{THz} is the azimuthal order of the generated THz light, and m_1 and m_2 are those of the pump light. The Au grating on top of the Si microdisk out-couples the confined THz light into free space. The angular phase-matching condition[35] requires the radiated THz light to obey

$$l = m_{THz} - q \qquad (2)$$

where l is the topological charge of the radiated light and q is the number of the grating elements. These two equations lead to

$$l = m_1 - m_2 - q \qquad (3)$$

which provides the basis for controlling the topological charge l in this work. For a given device where q is fixed, l can be tuned by adjusting the value of $m_1 - m_2$. As indicated in Fig. 2b, this work chooses to demonstrate the tuning of l by fixing m_1 (i.e. fixing λ_1) and changing m_2 (i.e. changing λ_2).

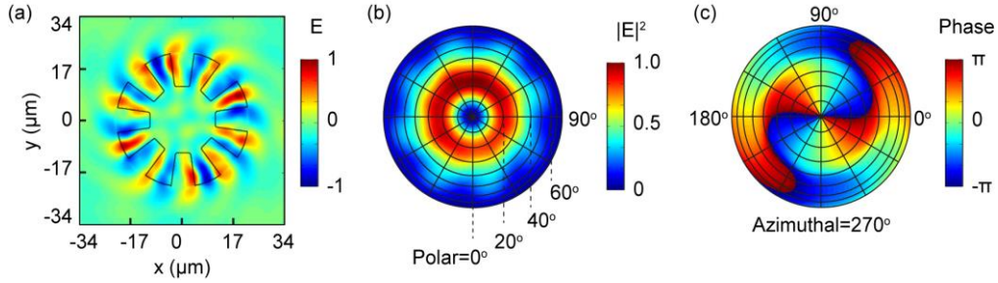

Fig. 3. THz generation with topological charge l = 2. (a) The z component of the THz electric field in the middle plane of the Si microdisk. (b,c) The intensity and phase of the THz radiation in the far field, covering the whole upper hemisphere with the polar angle ranging from 0° to 90° and the azimuthal angle from 0° to 360°. The origin of the polar coordinates is at the centre of the Si microdisk. The in-plane directions of +x (i.e. the light propagation direction in the straight waveguide) and +y correspond to azimuthal angles of 0° to 90°, respectively.

To numerically verify the analysis above, Fig. 3 shows the output properties of the device, with it functioning at l = 2. The input light waves are set at two microring resonances, with wavelengths of λ_1 = 1488.56 nm and λ_2 = 1582.75 nm. They generate a THz wave at ω_{THz} = 11.99 THz (wavelength λ_{THz} = 25.0 μm) based on the energy conservation in the nonlinear process. They also have $m_1 - m_2 = 10$, the number of free spectral ranges (FSRs) between them in Fig. 2b. As predicted by Eq. (1), this value is also the azimuthal order of the whispering gallery mode for the generated THz light. This prediction is confirmed by the results in Fig. 3a, where the near-field distribution in the Si microdisk shows 10 cycles along the circumference of the microdisk. Figs. 3b and 3c show the intensity and phase of the THz light in the far field, respectively. Every point on these two maps has a radial distance of one meter from the centre of the microdisk. Typical features of vortex beams are clearly revealed in the two figures: the intensity has a shape of a doughnut, and the phase has azimuthal dependence. Because of the side-pumping configuration, the intensity distribution in Fig. 3b deviates from having perfect rotational symmetry, but the deviation is very small. Along a circle enclosing the centre of the map in Fig. 3c, the total phase evolves by twice of 2π, confirming that l = 2.

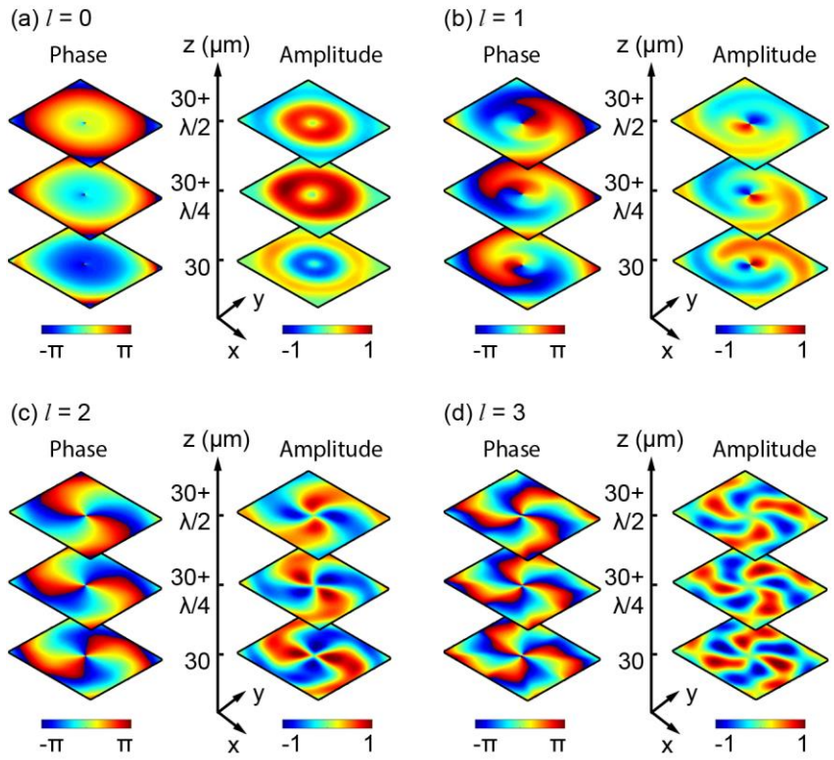

Fig. 4. Azimuthal components of the emitted THz light, with the device producing topological charges of (a) 0, (b) 1, (c) 2 and (d) 3. For each operation mode, the left and the right columns show the phase and the amplitude of the field, respectively. Each map occupies an area of 40 μm × 40 μm. The distance between adjacent maps is $\lambda_{THz}/4$, and the lowest plane is 30 μm above the centre of the microdisk. The amplitude in each map is normalised against the maximal value of the corresponding set of three maps.

For further verification of Eqs. (1)-(3), Fig. 4 compares four different operation modes of the emitter. For all the four beams, the radial index is zero in the Laguerre-Gaussian basis, and only the azimuthal component is shown here.[45] As indicated in Fig. 2b, λ_1 is fixed at λ_1 = 1488.56 nm, while λ_2 chooses the value of 1562.89 nm, 1572.76 nm, 1582.75 nm and 1592.89 nm in Figs. 4(a), 4(b), 4(c) and 4(d), respectively. The topological charge is predicted to range from 0 to 4 based on Eqs. (1)-(3), and it is confirmed by the results in Fig. 4. For each value of *l*, the azimuthal components of the radiated THz field are plotted at three different planes. The inter-plane distance is $\lambda_{THz}/4$, where λ_{THz} varies with the value of *l*.

A profound contrast is observed between the non-vortex beam (Fig. 4a) and the vortex beams (Figs. 4b-4d): both the phase and the amplitude are twisted in the latter, while no such feature is discernible in the former. The small features very close to the centre of the phase maps of Fig. 4a are attributed to numerical errors, as the local field intensity is almost zero. It is worth noting that the doughnut-shaped amplitude profile seen in Fig. 4a does not imply the existence of a finite topological charge, and similar features have been reported previously in non-vortex beams produced by linear vortex beam emitters.[36]

In contrast to Fig. 4a, the beams in Figs. 4b-4d all carry a finite value of topological charge l. The value of l is related to the twist of the fields and can be retrieved from the maps by using two different methods. The first method is to trace the rotation of the field in a xy plane: along a circle centred on the beam axis, the absolute value $|l|$ equals the cycle number of the phase or the amplitude, and the sign of l determines the direction (either clockwise or anti-clockwise) that the phase increases. The second method is to trace the rotation of the field along the z direction: the field rotates by $2\pi/|l|$ for a distance of λ, and the sign of l determines the rotation direction for both the phase and the amplitude.

V. Output spectra of three different designs

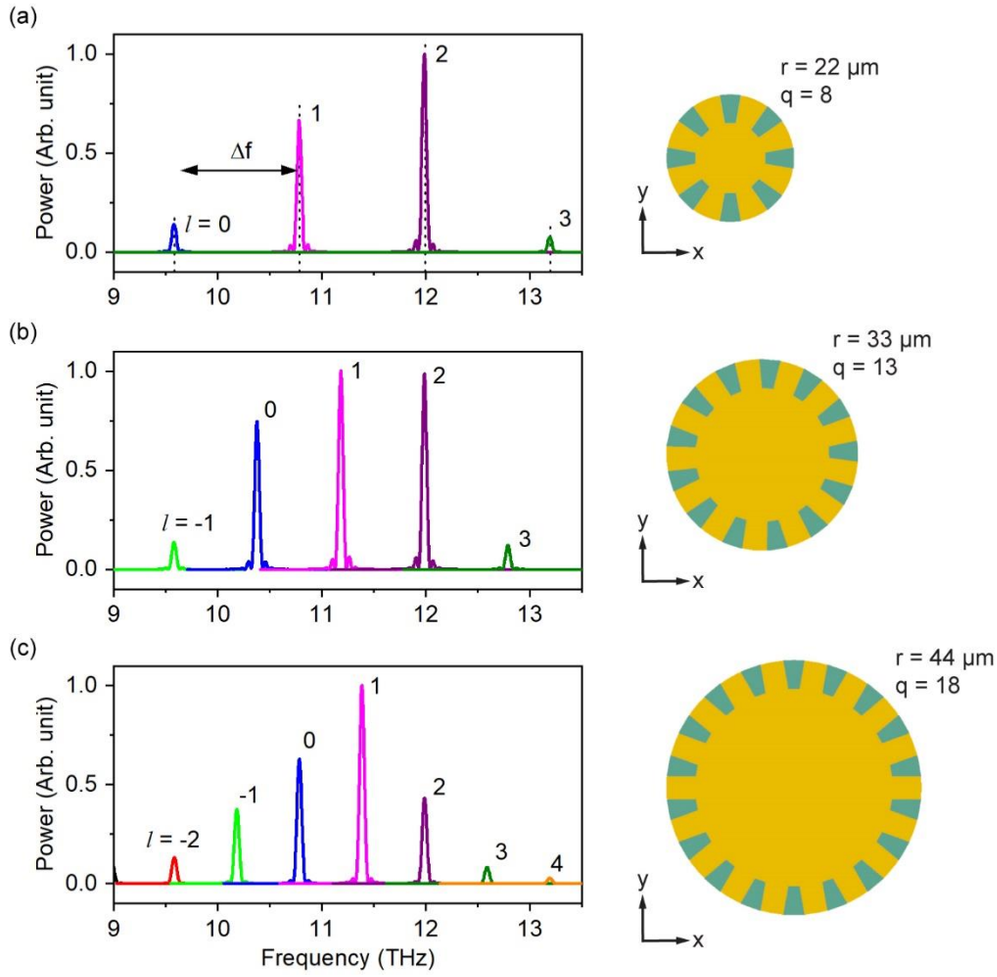

Fig. 5. Influences of planar microstructures on the output spectra for three different designs. The diameter of the Si microdisk r and the number of grating elements q are (a) r = 22 μm, q = 8 (the design discussed in previous figures), (b) r = 33 μm, q = 13, and (c) r = 44 μm, q = 18. In panel (a), central peak positions calculated using energy conservation in the difference-frequency generation are indicated by vertical dashed lines. In panel (c), the peak of l = -3 is slightly outside the spectral range presented here, with its central frequency at 8.98 THz. In all the panels, a frequency shift Δf accompanies a unit change in the topological charge. The spectra in each panel are normalised against the highest output power of the corresponding design. For all the designs, the straight waveguide is along the x direction.

Figure 5a shows the output spectra of the device in the frequency range from 9 THz to 13.5 THz. As l changes from 0 to 3, the peak frequency changes by 3.61 THz, from 9.58 THz at $l = 0$ to 13.19 THz at $l = 3$. This change originates from the energy conservation in the difference-frequency generation and follows the change of λ_2. The output power also depends on l. With both input light set at a test value of 10 W, the output reaches the highest value of 2.0×10^{-5} W at $l = 2$, and drops to 14% of this value at $l = 0$ and 8% at $l = 3$. This change in output power is directly related to the change in frequency, as the latter affects key characteristics such as light confinement of the microdisk and phase matching of the nonlinear process. All the peaks show a finite width, and some have small but discernible side bands. These features are artefacts associated with the FDTD method; both the peak width and the sidebands become smaller with increasing the simulation time (i.e. with waves better approximating perfect, monochromatic waves).

For this design architecture, a change in output frequency always accompanies a change in the topological charge due to the difference-frequency generation. Nevertheless, the magnitude of the frequency change can be controlled by modifying the planar size of the design. As long as the pump wavelengths (λ_1 and λ_2, both ~1.5 μm in the current design) are significantly larger than the FSR (~10 nm in the current design), the frequency change Δf that accompanies a unit change in l (i.e. $\Delta l = \pm 1$) is approximately

$$\Delta f \approx c \times \mathrm{FSR} / (\lambda_1 \times \lambda_2) \approx c \times \mathrm{FSR} / \lambda^2 \quad (4)$$

where c is the speed of light, and λ is the average of λ_1 and λ_2. For a microring resonator, the FSR is inversely proportional to the round trip length along the microring.[29] If the radius r is significantly larger than the width of the waveguide, the FSR can be approximated as

$$\mathrm{FSR} \approx \lambda^2 / (n_g \times 2 \times \pi \times r) \quad (5)$$

where n_g is the group velocity. This leads to the conclusion that by adjusting the radius of the microring, Δf can be controlled as

$$\Delta f \approx c / (n_g \times 2 \times \pi \times r) \quad (6)$$

The value of Δf scales inversely with the radius of the microring r.

To numerically verify this conclusion, the planar dimensions of the emitter are modified and the output spectra are shown in Figs. 5b and 5c. From the current design (Fig. 5a), the radii of the microring, defined from the middle of the waveguide, and the Si microdisk are increased by 50% in Fig. 5b, reaching 28.77 μm and 33 μm, respectively. For the third design in Fig. 5c, the increase is 100%, and the radii of the microring and the Si microdisk are 38.36 μm and 44 μm, respectively. In order to create similar values of l in the same frequency range for the three designs, the element number of the Au grating is increased from q =8 in Fig. 5a to 13 and 18 in Figs. 5b and 5c, respectively. All the other dimensions are the same for these three designs.

For the two new designs, the output spectra and the topological charges are calculated using the same methods discussed above (see Fig. S3 in the Supplementary Material for transmission spectra). Figure 5 compares the three designs in the same frequency range from 9 THz to 13.5 THz. The number of peaks is 4, 5 and 7 in Figs. 5a, 5b and 5c, respectively, increasing with the planar size of the emitter. The frequency difference between adjacent peaks Δf shows the opposite trend of change, which is 1.20 THz, 0.80 THz and 0.60 THz in Figs. 5a, 5b and 5c, respectively. To compare these values with results obtained from Eq. (6), the group velocity n_g is calculated at a representative wavelength of 1550 nm. The value shows a very small variation with the design, and it is 2.07, 2.06 and 2.09 for the designs in Figs. 5a, 5b and 5c, respectively. The analytical values of Δf obtained from Eq. (6) are consequently 1.20 THz, 0.80 THz and 0.60 THz for the three designs, matching very well with the values obtained directly from Fig. 5.

VI. Conclusion

To conclude, we have demonstrated a THz vortex beam emitter via numerical simulation. The emitter consists of a $LiNbO_3$ microring for difference-frequency generation, a Si microdisk for near-field confinement of the generated THz, and a Au second-order top grating for creation of topological charge. The device is pumped by two infrared light beams from a coupling waveguide, and emits THz light vertically into free space. The value of the topological charge can be tuned by changing the wavelengths of the incident light, and ranges from -2 to 4 in the simulated frequency range from 9 THz to 13.5 THz

for one of the three designs. The output spectra, in particular the frequency change that is associated with the change in topological charge, can be adjusted by tuning the planar dimensions of the emitter. As a proof-of-principle demonstration, this work concentrates on the topological charge and the frequency shift, while parameters such as conversion efficiency, including its balance among multiple output spectra peaks, could be further improved by exploring the vertical dimensions (e.g. via creating high-quality THz whispering-gallery modes).[46] The emitter has a planar dimension that is comparable to its functional wavelengths, and has the capability to impart a tuneable topological charge on a freely propagating THz light beam. These features can prove useful in a range of emerging THz applications such as THz wireless communications and electron acceleration.

Supplementary material

See the supplementary material for representative permittivity values used in the numerical simulation, planar dimensions of the smallest device, influence of the straight waveguide on THz generation, and the linear transmission spectra of the two larger devices.

Acknowledgements

This research was supported by the Royal Society (projects IEC\R3\183071 and IES\R3\183086) and the Engineering and Physical Sciences Research Council, UK (project EP/R005303/1).

Data availability statement

The data that support the findings will be available in the University of Southampton's ePrints research repository following an embargo from the date of publication.

References

1. A. M. Yao and M. J. Padgett, "Orbital angular momentum: origins, behavior and applications," Adv. Opt. Photon. **3**, 161-204 (2011).
2. J. Leach, E. Yao, and M. J. Padgett, "Observation of the vortex structure of a non-integer vortex beam," New Journal of Physics **6**, 71 (2004).

3. W. Brullot, M. K. Vanbel, T. Swusten, and T. Verbiest, "Resolving enantiomers using the optical angular momentum of twisted light," Science Advances **2**, e1501349 (2016).
4. A. A. Sirenko, P. Marsik, C. Bernhard, T. N. Stanislavchuk, V. Kiryukhin, and S. W. Cheong, "Terahertz Vortex Beam as a Spectroscopic Probe of Magnetic Excitations," Physical Review Letters **122**, 237401 (2019).
5. M. Ritsch-Marte, "Orbital angular momentum light in microscopy," Philosophical Transactions of the Royal Society A: Mathematical, Physical and Engineering Sciences **375**, 20150437 (2017).
6. M. Padgett and R. Di Leonardo, "Holographic optical tweezers and their relevance to lab on chip devices," Lab on a Chip **11**, 1196-1205 (2011).
7. J. Wang, J.-Y. Yang, I. M. Fazal, N. Ahmed, Y. Yan, H. Huang, Y. Ren, Y. Yue, S. Dolinar, M. Tur, and A. E. Willner, "Terabit free-space data transmission employing orbital angular momentum multiplexing," Nature Photonics **6**, 488-496 (2012).
8. H. Ren, X. Li, Q. Zhang, and M. Gu, "On-chip noninterference angular momentum multiplexing of broadband light," Science **352**, 805-809 (2016).
9. S. Ge, P. Chen, Z. Shen, W. Sun, X. Wang, W. Hu, Y. Zhang, and Y. Lu, "Terahertz vortex beam generator based on a photopatterned large birefringence liquid crystal," Opt. Express **25**, 12349-12356 (2017).
10. R. Imai, N. Kanda, T. Higuchi, K. Konishi, and M. Kuwata-Gonokami, "Generation of broadband terahertz vortex beams," Optics Letters **39**, 3714-3717 (2014).
11. Y. Gorodetski, A. Drezet, C. Genet, and T. W. Ebbesen, "Generating Far-Field Orbital Angular Momenta from Near-Field Optical Chirality," Physical Review Letters **110**, 203906 (2013).
12. J. He, X. Wang, D. Hu, J. Ye, S. Feng, Q. Kan, and Y. Zhang, "Generation and evolution of the terahertz vortex beam," Opt. Express **21**, 20230-20239 (2013).
13. Y. Yang, W. Wang, P. Moitra, I. I. Kravchenko, D. P. Briggs, and J. Valentine, "Dielectric Meta-Reflectarray for Broadband Linear Polarization Conversion and Optical Vortex Generation," Nano Letters **14**, 1394-1399 (2014).

14. X. Ma, M. Pu, X. Li, C. Huang, Y. Wang, W. Pan, B. Zhao, J. Cui, C. Wang, Z. Zhao, and X. Luo, "A planar chiral meta-surface for optical vortex generation and focusing," Scientific Reports **5**, 10365 (2015).
15. D. Hakobyan, H. Magallanes, G. Seniutinas, S. Juodkazis, and E. Brasselet, "Tailoring Orbital Angular Momentum of Light in the Visible Domain with Metallic Metasurfaces," Advanced Optical Materials **4**, 306-312 (2016).
16. X. Wang, Z. Nie, Y. Liang, J. Wang, T. Li, and B. Jia, "Recent advances on optical vortex generation," Nanophotonics **7**, 1533-1556 (2018).
17. S. S. Dhillon et al, "The 2017 terahertz science and technology roadmap," J. Phys. D: Appl. Phys. **50**, 043001 (2017).
18. I. F. Akyildiz, J. M. Jornet, and C. Han, "Terahertz band: Next frontier for wireless communications," Phys. Commun. 12, 16-32 (2014).
19. E. A. Nanni, W. R. Huang, K.-H. Hong, K. Ravi, A. Fallahi, G. Moriena, R. J. Dwayne Miller, and F. X. Kärtner, "Terahertz-driven linear electron acceleration," Nature Communications **6**, 8486 (2015).
20. L. Ju, B. Geng, J. Horng, C. Girit, M. Martin, Z. Hao, H. A. Bechtel, X. Liang, A. Zettl, Y. R. Shen, and F. Wang, "Graphene plasmonics for tunable terahertz metamaterials," Nature Nanotechnology **6**, 630-634 (2011).
21. C. W. Berry, N. Wang, M. R. Hashemi, M. Unlu, and M. Jarrahi, "Significant performance enhancement in photoconductive terahertz optoelectronics by incorporating plasmonic contact electrodes," Nature Communications **4**, 1622 (2013).
22. T. Nagatsuma, G. Ducournau, and C. C. Renaud, "Advances in terahertz communications accelerated by photonics," Nature Photonics **10**, 371-379 (2016).
23. G. D. Boyd, T. J. Bridges, M. A. Pollack, and E. H. Turner, "Microwave Nonlinear Susceptibilities Due to Electronic and Ionic Anharmonicities in Acentric Crystals," Physical Review Letters **26**, 387-390 (1971).

24. C. Staus, T. Kuech, and L. McCaughan, "Continuously phase-matched terahertz difference frequency generation in an embedded-waveguide structure supporting only fundamental modes," Opt. Express **16**, 13296-13303 (2008).
25. S. B. Bodrov, A. N. Stepanov, M. I. Bakunov, B. V. Shishkin, I. E. Ilyakov, and R. A. Akhmedzhanov, "Highly efficient optical-to-terahertz conversion in a sandwich structure with $LiNbO_3$ core," Opt. Express **17**, 1871-1879 (2009).
26. B. N. Carnio and A. Y. Elezzabi, "Enhanced broadband terahertz radiation generation near the reststrahlen band in sub-wavelength leaky-mode $LiNbO_3$ waveguides," Optics Letters **43**, 1694-1697 (2018).
27. G. Poberaj, H. Hu, W. Sohler, and P. Günter, "Lithium niobate on insulator (LNOI) for micro-photonic devices," Laser & Photonics Reviews **6**, 488-503 (2012).
28. M. Zhang, C. Wang, R. Cheng, A. Shams-Ansari, and M. Lončar, "Monolithic ultra-high-Q lithium niobate microring resonator," Optica **4**, 1536-1537 (2017).
29. W. Bogaerts, P. De Heyn, T. Van Vaerenbergh, K. De Vos, S. Kumar Selvaraja, T. Claes, P. Dumon, P. Bienstman, D. Van Thourhout, and R. Baets, "Silicon microring resonators," Laser & Photonics Reviews **6**, 47-73 (2012).
30. D. V. Strekalov, C. Marquardt, A. B. Matsko, H. G. L. Schwefel, and G. Leuchs, "Nonlinear and quantum optics with whispering gallery resonators," Journal of Optics **18**, 123002 (2016).
31. A. I. Zhmakin, "Enhancement of light extraction from light emitting diodes," Physics Reports **498**, 189-241 (2011).
32. Y. Rao, W. Yang, C. Chase, M. C. Y. Huang, D. P. Worland, S. Khaleghi, M. R. Chitgarha, M. Ziyadi, A. E. Willner, and C. J. Chang-Hasnain, "Long-Wavelength VCSEL Using High-Contrast Grating," IEEE Journal of Selected Topics in Quantum Electronics **19**, 1701311 (2013).
33. L. Mahler, A. Tredicucci, F. Beltram, C. Walther, J. Faist, B. Witzigmann, H. E. Beere, and D. A. Ritchie, "Vertically emitting microdisk lasers," Nature Photonics **3**, 46-49 (2009).
34. Y. Jin, L. Gao, J. Chen, C. Wu, J. L. Reno, and S. Kumar, "High power surface emitting terahertz laser with hybrid second- and fourth-order Bragg gratings," Nature Communications **9**, 1407 (2018).

35. X. Cai, J. Wang, M. J. Strain, B. Johnson-Morris, J. Zhu, M. Sorel, J. L. O'Brien, M. G. Thompson, and S. Yu, "Integrated Compact Optical Vortex Beam Emitters," Science **338**, 363-366 (2012).
36. S. A. Schulz, T. Machula, E. Karimi, and R. W. Boyd, "Integrated multi vector vortex beam generator," Opt. Express **21**, 16130-16141 (2013).
37. M. J. Strain, X. Cai, J. Wang, J. Zhu, D. B. Phillips, L. Chen, M. Lopez-Garcia, J. L. O'Brien, M. G. Thompson, M. Sorel, and S. Yu, "Fast electrical switching of orbital angular momentum modes using ultra-compact integrated vortex emitters," Nature Communications **5**, 4856 (2014).
38. P. Miao, Z. Zhang, J. Sun, W. Walasik, S. Longhi, N. M. Litchinitser, and L. Feng, "Orbital angular momentum microlaser," Science **353**, 464-467 (2016).
39. A. Z. Al-Attili, D. Burt, Z. Li, N. Higashitarumizu, F. Y. Gardes, K. Oda, Y. Ishikawa, and S. Saito, "Germanium vertically light-emitting micro-gears generating orbital angular momentum," Opt. Express **26**, 34675-34688 (2018).
40. N. Carlon Zambon, P. St-Jean, M. Milićević, A. Lemaître, A. Harouri, L. Le Gratiet, O. Bleu, D. D. Solnyshkov, G. Malpuech, I. Sagnes, S. Ravets, A. Amo, and J. Bloch, "Optically controlling the emission chirality of microlasers," Nature Photonics **13**, 283-288 (2019).
41. M. A. Ordal, R. J. Bell, R. W. Alexander, L. L. Long, and M. R. Querry, "Optical properties of Au, Ni, and Pb at submillimeter wavelengths," Applied Optics **26**, 744-752 (1987).
42. E. D. Palik, Handbook of optical constants of solids (Academic press, 1998).
43. L.-W. Luo, G. S. Wiederhecker, J. Cardenas, C. Poitras, and M. Lipson, "High quality factor etchless silicon photonic ring resonators," Opt. Express **19**, 6284-6289 (2011).
44. J. U. Fürst, D. V. Strekalov, D. Elser, A. Aiello, U. L. Andersen, C. Marquardt, and G. Leuchs, "Low-Threshold Optical Parametric Oscillations in a Whispering Gallery Mode Resonator," Physical Review Letters **105**, 263904 (2010).
45. N. K. Fontaine, R. Ryf, H. Chen, D. T. Neilson, K. Kim, and J. Carpenter, "Laguerre-Gaussian mode sorter," Nature Communications **10**, 1865 (2019).
46. D. W. Vogta and R. Leonhardt, "Ultra-high Q terahertz whispering-gallery modes in a silicon resonator," APL Photonics **3**, 051702 (2018).

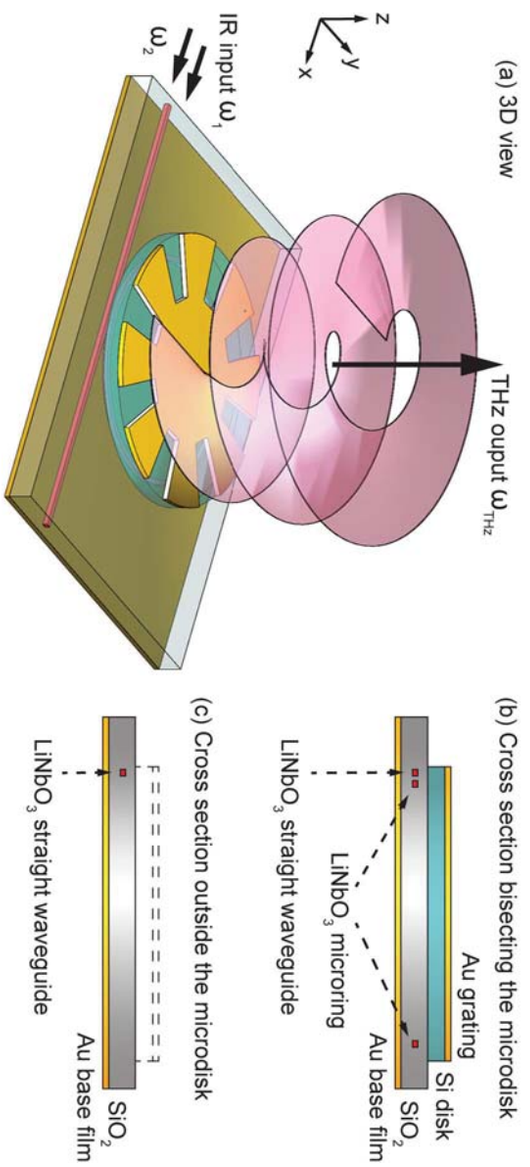

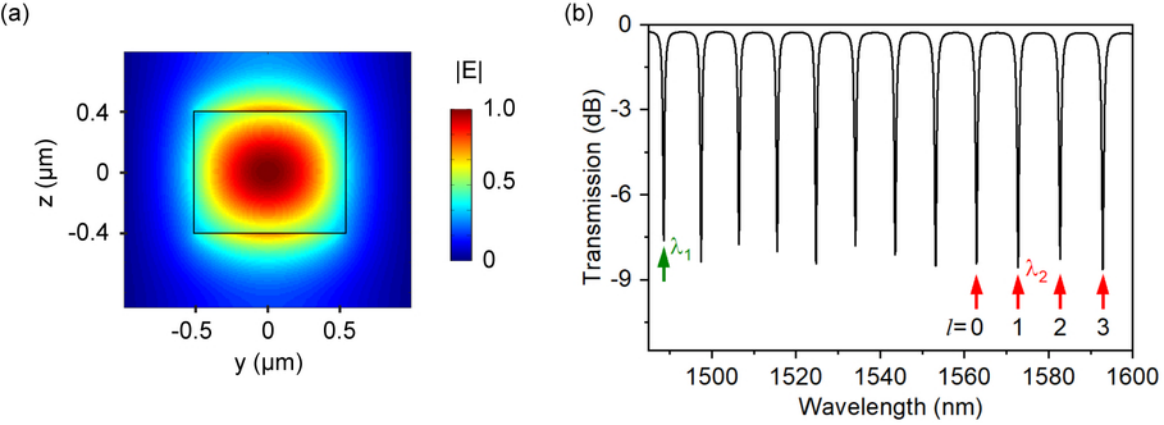
(a)
|E|
1.0
0.5
0
0.4
0
-0.4
z (μm)
-0.5
0
0.5
y (μm)
(b)
0
-3
-6
-9
Transmission (dB)
λ-1
λ-2
l= 0
1
2
3
1500
1520
1540
1560
1580
1600
Wavelength (nm)

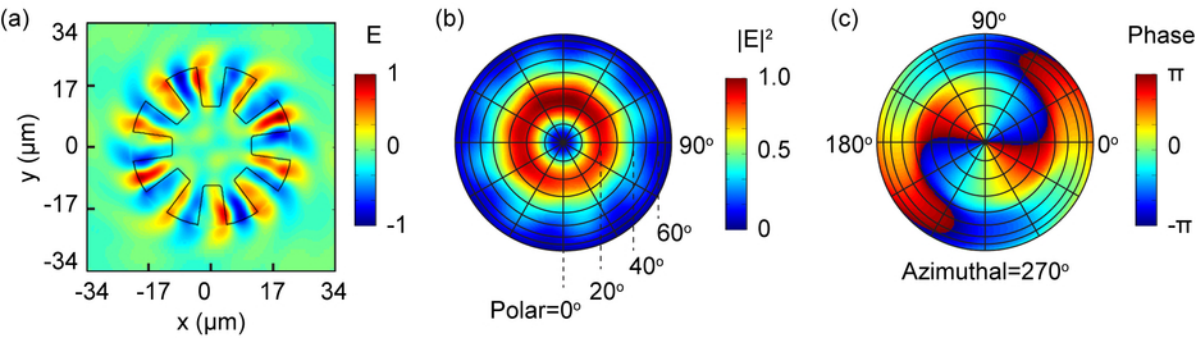
(a)
34
17
0
-17
-34
y (μm)
-34 -17 0 17 34
x (μm)
E
1
0
-1
(b)
90°
60°
40°
20°
Polar=0°
|E|²
1.0
0.5
0
(c)
90°
180°
0°
Azimuthal=270°
Phase
π
0
-π